Research Square

Preprints are preliminary reports that have not undergone peer review.
They should not be considered conclusive, used to inform clinical practice,
or referenced by the media as validated information.

A multifunctional self-assembled monolayer for perovskite lasing diodes

Chuanjiang Qin

cjqin@ciac.ac.cn

Changchun Institute of Applied Chemistry, Chinese Academy of Sciences https://orcid.org/0000-0002-6927-2544

Wei Yuan

Chinese Academy of Sciences

Wenping Wu

Changchun Institute of Applied Chemistry, Chinese Academy of Sciences

Nobuhiro Takeishi

Kyushu University

Atula S. D. Sandanayaka

Faculty of Applied Sciences, Sabaragamuwa University of Sri Lanka

Wei Zhou

Changchun Institute of Applied Chemistry, Chinese Academy of Sciences

Binhe Li

Changchun Institute of Applied Chemistry, Chinese Academy of Sciences

Helong Zhu

Changchun Institute of Applied Chemistry, Chinese Academy of Sciences

Dezhong Zhang

Changchun Institute of Applied Chemistry https://orcid.org/0000-0002-9878-6552

Pengcheng Li

College of Chemistry, Central China Normal University

Lixiang Wang

Central China Normal University

Chihaya Adachi

Kyushu University

Ifor Samuel

University of St Andrews https://orcid.org/0000-0001-7821-7208

Physical Sciences - Article

Keywords:

Posted Date: October 30th, 2026

DOI: https://doi.org/10.21203/rs.3.rs-11400196/v1

License: This work is licensed under a Creative Commons Attribution 4.0 International License.
Read Full License

Additional Declarations: There is **NO** Competing Interest.

A multifunctional self-assembled monolayer for perovskite lasing diodes

Wei Yuan[1,2], Wenping Wu[1,2], Nobuhiro Takeishi[4], Atula S. D. Sandanayaka[5], Wei Zhou[1], Binhe Li[1,2], Helong Zhu[1], Dezhong Zhang[1], Pengcheng Li[6,7], Lixiang Wang[1,6,7*], Chihaya Adachi[4,*], Ifor D. W. Samuel[3,*], and Chuanjiang Qin[1,2,*]

[1] State Key Laboratory of Polymer Science and Technology, Changchun Institute of Applied Chemistry, Chinese Academy of Sciences, Changchun 130022, China

[2] School of Applied Chemistry and Engineering, University of Science and Technology of China, Hefei 230026, China

[3] Organic Semiconductor Centre, School of Physics and Astronomy, University of St Andrews, North Haugh, St Andrews, Fife, KY16 9SS, UK

[4] Department of Physical Sciences and Technology, Faculty of Applied Sciences, Sabaragamuwa University of Sri Lanka, Belihuloya 70140, Sri Lanka

[5] Center for Organic Photonics and Electronics Research, Kyushu University, Fukuoka 819-0395, Japan

[6] College of Chemistry, Central China Normal University, Wuhan, 430079, China.

[7] Wuhan Institute of Photochemistry and Technology, Wuhan, 430083, China.

Abstract

Perovskite lasing diodes (PeLDs) require charge transport, optical gain, resonant feedback and high-density electrical injection to be integrated within a single thin-film device. Conventional hole transport materials (HTM) can, however, introduce non-radiative recombination and optical loss in nanophotonic cavities. Here we develop RS-3, a self-assembled monolayer that acts as a multifunctional hole-transport contact. The ultrathin RS-3 layer reduces buried-interface loss, increases net modal gain and preserves the periodic profile of the distributed-feedback (DFB) cavity after deposition of the quasi-two-dimensional N2F8 gain layer, enabling us to realize room-temperature current-assisted lasing under synchronized optical–electrical co-injection. RS-3-based light-emitting diodes also show lower turn-on voltage, higher current density and higher luminance than poly(9-vinylcarbazole)-based controls. Under pulsed optical pumping, the complete device lases near 550 nm at a threshold of 28 μJ cm^{-2}. With synchronized optical–electrical co-injection, the threshold decreases monotonically to 19 μJ cm^{-2} as the pulsed current density increases to 1.30 kA cm^{-2}, with a minimum linewidth of 0.25 nm.

Introduction

PeLDs are promising thin-film coherent light sources for integrated photonics, high-resolution displays, optical communications and on-chip optoelectronics[1-3]. Quasi-two-dimensional perovskites are attractive gain media because their quantum-well-like energy landscape supports efficient exciton funneling, high radiative efficiency and stable lasing[4-10]. Among them, N2F8 has demonstrated a stable room-temperature continuous-wave lasing by triplet management in a DFB cavity, making it a suitable gain medium for pursuing current-injection PeLDs[11-13]. In typical perovskite DFB lasers, the carrier density required for optical gain and lasing is estimated to reach the 10^{18} cm^{-3} level[12,14-16]. Previous PeLDs have approached electrically injected carrier densities on the order of 10^{17} cm^{-3} around 230 K[17]. Subsequently, electrically assisted amplified spontaneous emission (ASE) was demonstrated in perovskite light-emitting diodes under combined optical and electrical excitation, showing that injected carriers can contribute to optical-gain[18]. More recently, demonstrations of indirect electrically driven perovskite lasing based on a dual distributed Bragg reflector, in which a bottom perovskite light-emitting diode optically pumps a top perovskite gain cavity, highlight the rapid progress of the field[19]. Direct-current perovskite polariton lasing has subsequently been demonstrated at 8 K using a $CsPbBr_3$ microplate embedded in an optical microcavity, establishing the feasibility of direct electrical pumping in a cryogenic strong-coupling regime[20]. Nevertheless, simultaneously integrating charge transport, optical gain, resonant feedback and high-density electrical injection within a single-junction, room-temperature thin-film laser diode remains an important challenge[3,18,20-22].

A polymer HTM was reported to reduce the ASE threshold of optically pumped perovskite lasers by regulating interfacial carrier dynamics[23]. However, conventional polymer HTMs such as poly(9-vinylcarbazole) (PVK) are less suited to PeLDs, because their long-chain nature and amorphous morphology can introduce optical loss and planarize nanoscale DFB gratings. Recently, a broad range of self-assembled monolayers (SAMs) have been successfully used as new types of HTM in

perovskite/organic solar cells and light-emitting diodes[24-32]. By virtue of their additional molecular dipole tuning and defect passivation functions, champion device performances were achieved[24-26,31]. However, to the best of our knowledge, SAMs have not been used for PeLDs, although theoretically they may promote gain formation, feedback cavity conformation and high-density charge injection[24,26-28,31,33].

Here, we developed a new multifunctional SAM RS-3 guided by our previous molecular design strategy on RS-2[26] for perovskite lasing. We replaced the phenoxazine core of RS-2 by bromine-substituted phenothiazine to lower the level of the highest occupied molecular orbital (HOMO), increase the refractive index, preserve the effective DFB corrugation, thereby matching with the photophysical properties of N2F8 gain. Compared with PVK-based controls, RS-3/N2F8 structures exhibit improved ASE and lasing characteristics. The RS-3 reduces the barrier of hole injection and accelerates radiative build-up under nanosecond electrical pulses, leading to higher PeLEDs performance. Finally, we realized room-temperature lasing under synchronized photoelectric co-injection, with the optical threshold decreasing monotonically from 28 to 19 μJ cm^{-2} as the pulsed electrical current density increased from 0 to 1.30 kA cm^{-2}. Our results establish SAM as an active photonic–electronic interface for developing single-stack optical and electrical pumping of perovskite lasers.

RS-3 SAM improves the optical gain budget of N2F8 films

The chemical structures of RS-3 and PVK are drawn in Fig. 1a. The synthesis routes and molecular characterization of RS-3 are shown in Supplementary Note 1 and Supplementary Fig. 1a–d. To understand their effects on the optical gain properties, we prepared the N2F8 gain film on the ITO substrates with self-assembled RS-3 and spin-coated PVK respectively. X-ray diffraction patterns and absorption spectra confirmed that the N2F8 phase and band-edge optical transitions are similar on PVK and RS-3 layers (Supplementary Fig. 2a, b). The optical differences below therefore mainly arise from buried-interface regulation rather than from a phase change in the quasi-2D perovskite polycrystalline films.

In Fig. 1b, RS-3/N2F8 film exhibits much stronger and sharper ASE peaks than PVK/N2F8 film. The ASE threshold decreases from 189 μJ cm^{-2} for PVK/N2F8 to 58 μJ cm^{-2} for RS-3/N2F8, while the linewidth narrows from 3.2 to 2.0 nm (Fig. 1c). Repeated measurements confirm that the lower ASE threshold is reproducible across RS-3/N2F8 films (Supplementary Fig. 2 c, d).

To distinguish optical amplification from propagation loss, we measured the net modal gain and waveguide loss. Variable-stripe-length measurements show that the net gain increases from 91 cm^{-1} for PVK/N2F8 to 188 cm^{-1} for RS-3/N2F8 (Fig. 1d). On the other hand, the propagation loss decreases from 44 to 4.3 cm^{-1} in the variable-distance measurements (Fig. 1e). Although RS-3 exhibits a higher effective refractive index than PVK over the measured spectral range (Supplementary Fig. 2e), the approximately 3-nm-thick RS-3 SAM is not expected to substantially alter the optical-mode confinement. The more favourable optical-gain budget of RS-3/N2F8 is therefore attributed primarily to reduced propagation loss and improved emissive properties.

To connect these macroscopic gain characteristics with excited-state dynamics, we performed pump-power-dependent femtosecond transient absorption (fs-TA) spectroscopy. The transient spectra are provided in Supplementary Note 3. The extracted fs-TA parameters are summarized in Fig. 1f. In PVK/N2F8, the SE-related signal appears only at 18.0 μW, with a fast depletion time of 23 ps and a fast-component fraction of 0.33. This delayed and weak SE-related pathway is consistent with carrier loss through traps and other non-radiative channels[34,35]. In contrast, RS-3/N2F8 already shows an SE-related feature at 9.5 μW, with a much faster depletion time of 1.5 ps and a dominant fast-component fraction of 0.86. These results indicate that RS-3 lowers the excitation density required to access an SE-active carrier population and renders the rapid SE-associated depletion pathway dominant.

RS-3/N2F8 retains 87% of its initial ASE intensity, whereas PVK/N2F8 remains only 24% after 600,000 laser shots (Supplementary Fig. 2f). The gain-budget summary further highlights the combined effect of RS-3: higher net gain, lower propagation loss,

narrower ASE linewidth, lower ASE threshold and improved operational stability (Fig. 1g).

We propose the following mechanism for enhanced ASE performance. RS-3 anchors to the oxide surface through its phosphonic-acid group, and its bromine- and methoxy-substituted phenothiazine framework forms an ultrathin molecular contact that reduces buried-interface trap-assisted loss of N2F8 gain film (Fig. 1h). This is evidenced by the lower propagation loss, higher net modal gain, improved ASE stability and earlier, faster SE dynamics of RS-3/N2F8. By contrast, the thicker PVK interlayer is more susceptible to interfacial disorder and optical loss, consistent with the weaker ASE response, higher propagation loss and delayed SE onset in PVK/N2F8 (Fig. 1i). RS-3 therefore promotes population transfer into the SE-active pathway, whereas PVK is prone to causing more photoexcited carriers lost before efficient SE is established.

RS-3 SAM preserves DFB and reduces optical lasing thresholds

We fabricated ITO/DFB/PVK or RS-3/N2F8 devices for optically pumped lasers. The left schematics of Fig. 2a are the proposed N2F8 profiles on PVK- and RS-3-based DFB substrates, and the right atomic force microscopy (AFM) images show the corresponding surface morphologies. The PVK-based stack appears smoother, indicating that the long-chain polymer partially planarizes the patterned substrate and reduces the effective modulation in the cavity. In contrast, the RS-3-based stack retains a clearer periodic morphology because the ultrathin SAMs anchors and follows the underlying ITO/SiO_2 grating. AFM line profiles further confirm that RS-3 more effectively preserves the grating corrugation than PVK (Fig. 2b). The contact angle decreases from 20° on PVK to 10° on RS-3, indicating stronger affinity between the RS-3-modified surface and the N2F8 precursor (Supplementary Fig. 3a,b). This benefits N2F8 to penetrate the channel of patterned substrate while retaining the nanoscale feedback structure.

Under pulsed optical excitation, both devices show narrow emission above the thresholds, but the lasing peak of PVK-based devices exhibits a blue-shift relative to that of RS-3 (Fig. 2c). This shift caused by a change in the effective DFB geometry after PVK planarization. Importantly, the RS-3-based device gives a stronger lasing peak and a clearer far-field double slit pattern, indicating more efficient coupling between N2F8 and the preserved DFB mode. The optically pumped lasing threshold decreases from 57 μJ cm^{-2} for the PVK-based device to 24 μJ cm^{-2} for the RS-3-based device (Fig. 2d). The RS-3-based laser also shows a steeper intensity increase and a clearer linewidth collapse above threshold. Repeated measurements confirm the reproducibility of the low thresholds (Supplementary Fig. 3c,d).

The lower threshold is further supported by better emissive quality. The photoluminescence quantum yield increases from 75% for PVK/N2F8 to 91% for RS-3/N2F8 (Supplementary Fig. 3e). Time-resolved photoluminescence and recombination-rate analyses show a higher radiative rate and a lower non-radiative rate in the case of RS-3/N2F8 gain film (Fig. 2e,f and Supplementary Table 1).

RS-3 SAM promotes carrier injection and fast radiative build-up

The HTM must support efficient electrical injections under the pulsed high-current-density relevant to laser-diode operation[36,37]. We fabricated PeLEDs with the structure of ITO/PVK or RS-3/N2F8/PO-T2T/LiF/Al/Ag. The energy-level diagram shows that RS-3 has better matched HOMO level (-5.6 eV) with the N2F8 valence band (-5.7 eV), reducing the hole-injection barrier (Fig. 3a, Supplementary Fig. 4 and Table 2). Its molecular-scale thickness can also provide a shorter tunnelling path for hole injections.

The RS-3-based PeLEDs show a higher external quantum efficiency (EQE) than the PVK-based devices over a broad current-density range, with the maximum EQE increasing from 5.1% to 9.3% (Fig. 3b). The turn-on voltage decreases from 3.5 to 1.9 V, the maximum current density increases from 214 to 663 mA cm^{-2}, and the maximum luminance rises from 9,296 to 71,765 cd m^{-2} after replacing PVK with RS-3 (Fig. 3c).

These changes indicate more efficient carrier supply and radiative recombination in the RS-3-based PeLEDs.

We performed time-resolved electroluminescence (TREL) to probe the transient carrier injection and EL emission processes, with the analysis method described in Supplementary Note 4. Under a 60 V pulse with a width of 240 ns, the RS-3-based diode reaches its emission maximum faster than the PVK-based diode (Fig. 3d). The rise time decreases from 144 to 90 ns, convincing that RS-3 accelerates radiative build-up under pulsed electrical excitation.

Pulse-width-dependent measurements show that the RS-3 PeLED has shorter decay times than the PVK-based device across the tested pulse widths (Fig. 3e and Supplementary Fig. 5). At 240 ns, the decay time decreases from 116 ns for PVK to 34 ns for RS-3. The faster decay indicates more rapid carrier depletion after the electrical pulse and reduced residual carrier accumulation in the device.

The rise-time trend gives the same conclusion. From 80 to 240 ns, the RS-3-based diode consistently exhibits shorter rise times than the PVK-based diode (Fig. 3f). The extracted rise and decay parameters are summarized in Supplementary Table 3. Those results indicate that the RS-3 HTL enables faster carrier injection and quicker conversion of injected carriers into EL emissions.

RS-3 SAM enables room-temperature photoelectric co-injection lasing

We integrated RS-3 into a complete PeLD architecture of glass/ITO/SiO_2 DFB/RS-3/N2F8/PO-T2T/LiF/Al/Ag (Fig. 4a,b). The cross-sectional image of scanning electron microscopy confirms that the multilayer stack is formed and that the periodic DFB profile is still present after deposition of the gain layer, electron-transporting layer and top electrode (Fig. 4b). Thus, the conformal RS-3 interface preserves the feedback structure in PeLDs (compared to the PVK-PeLDs in the Supplementary Fig. 6a).

The device operated at room temperature under pulsed electrical excitation up to a peak current density of 1.42 kA cm^{-2} (Fig. 4c and Supplementary Fig. 6b). At the highest current density, the electroluminescence spectrum showed a grating-selected feature near 550 nm superimposed on a broad background, with a full-spectrum FWHM of approximately 26 nm, while the projected emission remained spatially broad on a screen positioned 30 cm from the device (Supplementary Fig. 7a). The emission was partially linearly polarized, with a degree of linear polarization of 46.5% and maximum intensity when the analyzer axis was parallel to the DFB grating grooves (Supplementary Fig. 8a), consistent with polarization-selective outcoupling by the one-dimensional second-order DFB grating. In the absence of a threshold-like transition under electrical excitation alone, we attribute these spectral and polarization characteristics to the grating and describe the emission as cavity-coupled electroluminescence rather than electrically driven lasing[38].

By contrast, the PVK-based control PeLD failed at approximately 180 A cm^{-2}, precluding subsequent photoelectric co-injection lasing measurements (Supplementary Fig. 6c,d). We then measured the same RS-3-based PeLD under pulsed optical excitation. The device shows a lasing peak near 550 nm with a threshold of 28 μJ cm^{-2}, accompanied by a narrow, vertically elongated projected emission pattern (Fig. 4d and Supplementary Fig. 7b). This confirms that the gain and feedback advantages of RS-3 remain effective after introducing the electron-transporting layer and top electrode. In contrast, the PVK-based PeLD has weaker cavity-coupled emission and a higher threshold (Supplementary Fig. 6e-f).

To realize lasing, we applied synchronized photoelectric co-injection (Supplementary Fig. 9). The PeLD was biased at a fixed pulsed electrical current density of 1.30 kA cm^{-2}, while a pulse laser excitation was input into the same device (Fig. 4e). The optical pulse was temporally positioned within the plateau region of the 240 ns electrical pulse, after the electrically injected carrier population had approached its quasi-steady-state value (Supplementary Fig. 6g).

Under co-injection, the emission evolves into a sharp lasing peak as the optical pump fluence increases, while a narrow vertical emission pattern is observed on a 20 cm × 10 cm screen positioned 30 cm from the device (Fig. 4e and Supplementary Fig. 7c). Under photoelectric co-injection, the degree of linear polarization increased from 46.5% to 79.3%, with the intensity maximum remaining parallel to the DFB grating grooves (Supplementary Fig. 8b), consistent with selective amplification of the grating-coupled TE-like mode. The spectra below and above threshold show a clear transition from broader cavity-coupled emission to a dominant narrow laser line (Fig. 4f). The light-output and linewidth analysis gives a co-injection threshold of 19 μJ cm^{-2}, with an abrupt intensity increase and linewidth collapse to 0.25 nm (Fig. 4g).

To directly test the current-density dependence, we measured pump-fluence-dependent emission at additional pulsed electrical current densities of 0.33, 0.68 and 1.07 kA cm^{-2} (Supplementary Fig. 10). The optical lasing threshold decreased monotonically with increasing electrical current density, falling from 28 μJ cm^{-2} without electrical injection to 19 μJ cm^{-2} at 1.30 kA cm^{-2} (Supplementary Fig. 11). This systematic dependence directly demonstrates that electrical injection progressively assists gain build-up and reduces the additional optical excitation required for lasing[17,18].

Carrier-density analysis provides an order-of-magnitude comparison of the optical and electrical excitation channels (Fig. 4h and Supplementary Note 5). Pure optical pumping at 28 μJ cm^{-2} corresponds to a fluence-equivalent density of 3.56×10^{18} cm^{-3}, whereas the co-injection threshold of 19 μJ cm^{-2} corresponds to 2.46×10^{18} cm^{-3}. An effective ABC model estimates an instantaneous electrically injected carrier density of 1.03×10^{18} cm^{-3} immediately before the optical pulse. Because this upper-bound estimate assumes $\eta_{\mathrm{inj}} = 1$ and differs temporally from the optical quantities, the values are not directly additive; their comparable scale is nevertheless consistent with electrically assisted gain build-up.

Conclusion

We developed a multifunctional RS-3 self-assembled monolayer for room-temperature PeLDs. The RS-3 SAM reduces buried-interface loss and facilitates the formation of a gain-active carrier population in N2F8. Its ultrathin and conformal architecture preserves the effective DFB geometry required for Bragg feedback. In the current injection device, its favorable energy alignment and ultrathin contact enable faster charge injection and generation of light under nanosecond electrical pulses. These coupled effects allow the complete PeLD to sustain high-density pulsed operation and realize lasing under synchronized photoelectric co-injection. Our results identify molecular-interface engineering as a route to electronically assisted gain in thin-film perovskite lasing devices.

References:

1. Sutherland, B. R. & Sargent, E. H. Perovskite photonic sources. *Nat. Photon.* **10**, 295–302 (2016).

2. Veldhuis, S. A. *et al.* Perovskite materials for light-emitting diodes and lasers. *Adv. Mater.* **28**, 6804–6834 (2016).

3. Lei, L. *et al*. Metal halide perovskites for laser applications. *Adv. Funct. Mater.* **31**, 2010144 (2021).

4. Xing, G. *et al.* Low-temperature solution-processed wavelength-tunable perovskites for lasing. *Nat. Mater.* **13**, 476–480 (2014).

5. Yuan, M. *et al.* Perovskite energy funnels for efficient light-emitting diodes. *Nat. Nanotechnol.* **11**, 872–877 (2016).

6. Wang, N. *et al.* Perovskite light-emitting diodes based on solution-processed self-organized multiple quantum wells. *Nat. Photon.* **10**, 699–704 (2016).

7. Zhao, B. *et al.* High-efficiency perovskite–polymer bulk heterostructure light-emitting diodes. *Nat. Photon.* **12**, 783–789 (2018).

8. Zhang, D. *et al.* Suppressing thermal quenching via defect passivation for efficient quasi-2D perovskite light-emitting diodes. *Light Sci. Appl.* **11**, 69 (2022).

9. Zhang, H. *et al.* 2D Ruddlesden–Popper perovskites microring laser array. *Adv. Mater.* **30**, 1706186 (2018).

10. Liu, S., *et al.* In-situ formation of oriented perovskite nanosheets with tailored optical dipoles enabling >30% EQE in pure-red LEDs. *Light Sci. Appl.* **15**, 163 (2026).

11. Qin, C. *et al.* Triplet management for efficient perovskite light-emitting diodes. *Nat. Photon.* **14**, 70–75 (2020).

12. Qin, C. *et al.* Stable room-temperature continuous-wave lasing in quasi-2D perovskite films. *Nature* **585**, 53–57 (2020).

13. Wagner, I. *et al.* Critical roles of ultrafast energy funneling and ultrafast singlet–triplet annihilation in quasi-2D perovskite optical gain mechanisms. *Adv. Mater.* **37**, 2419674 (2025).

14. Jia, Y. *et al.* Continuous-wave lasing in an organic–inorganic lead halide perovskite semiconductor. *Nat. Photon.* **11**, 784–788 (2017).

15. Li, Z. *et al.* Room-temperature continuous-wave operation of organometal halide perovskite lasers. *ACS Nano* **12**, 10968–10976 (2018).

16. Zhang, Q., Shang, Q., Su, R., Do, T. T. H. & Xiong, Q. Halide perovskite semiconductor lasers: materials, cavity design, and low threshold. *Nano Lett.* **21**, 1903–1914 (2021).

17. Grede, A. J., Cawthorn, R., Rand, B. P. & Giebink, N. C. Electrically assisted lasing in metal halide perovskite semiconductors. *ACS Photon.* **11**, 1851–1856 (2024).

18. Elkhouly, K. *et al.* Electrically assisted amplified spontaneous emission in perovskite light-emitting diodes. *Nat. Photon.* **18**, 132–138 (2024).

19. Zou, C. *et al.* Electrically driven lasing from a dual-cavity perovskite device. *Nature* **645**, 369–374 (2025).

20. Pushkarev, A. P. et al. Non-epitaxial perovskite polariton laser diode operating under direct current. *Nature* https://doi.org/10.1038/s41586-026-10824-w (2026).

21. Cho, C. *et al.* Electrical pumping of perovskite diodes: toward stimulated emission. *Adv. Sci.* **8**, 2101663 (2021).

22. Li, Z. *et al.* Highly bright perovskite light-emitting diodes enabled by retarded Auger recombination. *Nat. Commun.* **16**, 927 (2025).

23. Zhang, J. *et al.* Transport layer engineering toward lower threshold for perovskite lasers. *Adv. Mater.* **35**, 2300922 (2023).

24. Jia, L. *et al.* Efficient perovskite/silicon tandem with asymmetric self-assembly molecule. *Nature* **644**, 912–919 (2025).

25. Al-Ashouri, A. *et al.* Monolithic perovskite/silicon tandem solar cell with >29% efficiency by enhanced hole extraction. *Science* **370**, 1300–1309 (2020).

26. Wu, W. *et al.* Stable and uniform self-assembled organic diradical molecules for perovskite photovoltaics. *Science* **389**, 195–199 (2025).

27. Zhang, S. *et al.* Minimizing buried interfacial defects for efficient inverted perovskite solar cells. *Science* **380**, 404–409 (2023).

28. Chen, B. *et al.* Dual-function self-assembled molecules as hole-transport layers for thermally evaporated high-efficiency blue perovskite light-emitting diodes. *Adv. Mater.* **37**, 2411451 (2025).

29. Xie, Y. *et al.* Thiophene expanded self-assembled monolayer as hole transport layer for organic solar cells with efficiency of 20.78%. *Adv. Mater.* **37**, e02485 (2025).

30. Chen, X. *et al.* Perylenocarbazole-based polycyclic aromatic self-assembled monolayers with tailored electrostatic potentials for high-performance organic and perovskite solar cells. *Angew. Chem. Int. Ed.* https://doi.org/10.1002/anie.4031162 (2026).

31. Jiang, L. *et al.* Self-assembled monolayers facilitate simultaneous enhancements of external quantum efficiencies and circularly polarized luminescence dissymmetry factors for chiral perovskite red spin-light emitting diodes. *Adv. Sci.* **13***,* e12057 (2026).

32. Ullah, A. *et al.* Novel phenothiazine-based self-assembled monolayer as a hole selective contact for highly efficient and stable p–i–n perovskite solar cells. *Adv. Energy Mater.* **12**, 2103175 (2022).

33. Annavarapu, N. *et al.* Four-dimensional design space of high-Q second-order distributed feedback perovskite lasers. *Adv. Opt. Mater.* **12**, 2302496 (2024).

34. Yu, J. *et al.* Probing the spatial heterogeneity of carrier relaxation dynamics in $CH_3NH_3PbI_3$ perovskite thin films with femtosecond time-resolved nonlinear optical microscopy. *Adv. Opt. Mater.* **7**, 1901185 (2019).

35. Wu, C.-S. J., Olivati, A., Folpini, G., Wang, H. & Petrozza, A. Thin film stoichiometry and defects management for low threshold and air stable near-infrared perovskite laser. *Adv. Mater.* **37**, 2407652 (2025).

36. Kim, H. *et al.* Hybrid perovskite light emitting diodes under intense electrical excitation. *Nat. Commun.* **9**, 4893 (2018).

37. Zhao, L. *et al.* Nanosecond-pulsed perovskite light-emitting diodes at high current density. *Adv. Mater.* **33**, 2104867 (2021).

38. Samuel, I. D. W., Namdas, E. B. & Turnbull, G. A. How to recognize lasing. *Nat. Photon.* **3**, 546–549 (2009).

Acknowledgments This work was supported by the National Science Fund for Distinguished Young Scholars (grant T2425022), the Strategic Priority Research Program of the Chinese Academy of Sciences (XDB0520102), the National Natural Science Foundation of China (grant 22675285), the CAS Project for Young Scientists in Basic Research (grant YSBR-110).

Author Contributions C.Q. and W.Y. conceived the concept. W. Y., C.Q., W. W., A.S.D.S., W. Z., B. L. and D. Z. performed experiments and analyzed data. W. Y., N. T., A.S.D.S., and C.A. designed and fabricated DFB cavities. C.Q. and W.Y. prepared the manuscript. All authors discussed the results and commented on the manuscript. C. Q. and L. W. managed the projects.

Author Information Reprints and permissions information is available at www.nature.com/reprints. The authors declare no competing financial interests. Correspondence and requests for materials should be addressed to L.W. (lxwang@ccnu.edu.cn) C.A. (adachi@cstf.kyushu-u.ac.jp). I.D.W.S. (idws@st-andrews.ac.uk) and C.Q. (cjqin@ciac.ac.cn).

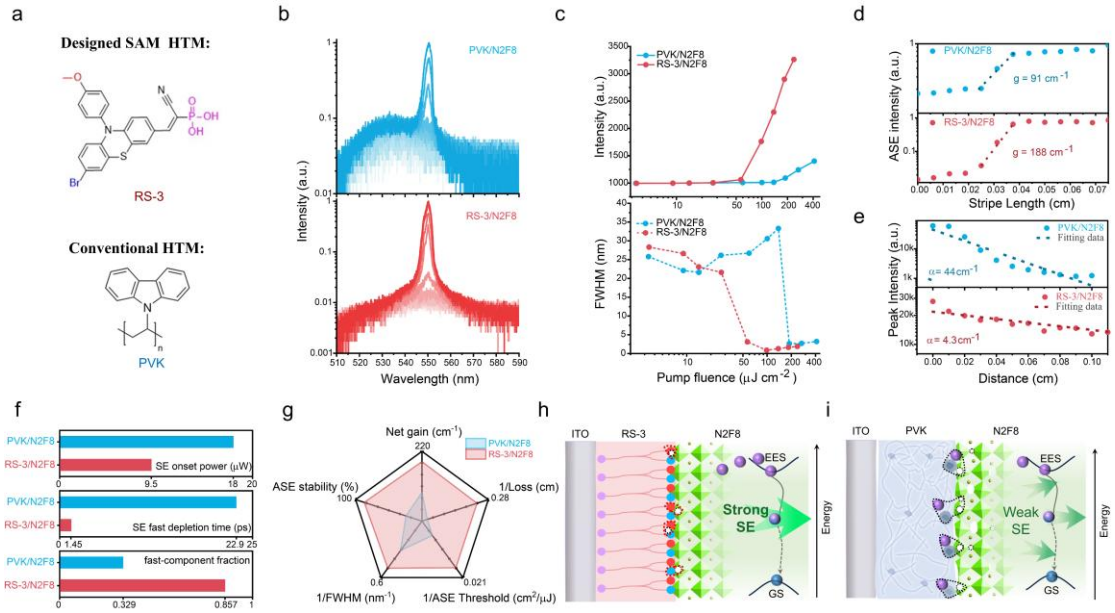


Figure 1. RS-3 improves the optical-gain budget and SE-associated carrier dynamics of N2F8 films.

a, Chemical structures of the SAM-forming hole-transport molecule RS-3 and the conventional polymeric hole-transport material PVK. **b,** Pump-fluence-dependent emission spectra of PVK/N2F8 (top) and RS-3/N2F8 (bottom) films. The pump fluences, increasing from the lightest to the darkest traces, are 3.3, 9.1, 14.2, 26.7, 59.7, 100, 138, 189, 268 and 412 μJ cm^{-2} for PVK/N2F8, and 3.4, 9.1, 14.1, 26.9, 56.9, 98.7, 138, 184 and 238 μJ cm^{-2} for RS-3/N2F8. **c,** Pump-fluence-dependent peak emission intensity (top) and full-width at half-maximum (FWHM; bottom) of PVK/N2F8 and RS-3/N2F8 films. The ASE threshold is identified from the concurrent nonlinear increase in emission intensity and spectral narrowing. **d,** Variable-stripe-length measurements and corresponding fits used to extract net modal gains. **e,** Variable-distance measurements and exponential fits used to determine propagation-loss coefficients. **f,** Comparison of the fs-TA-derived SE onset pump power, fast-depletion time and fast-component fraction. **g,** Radar-plot comparison of the net modal gain, reciprocal propagation loss, reciprocal ASE threshold, reciprocal ASE linewidth and ASE stability of the two films. **h,i,** Proposed interfacial mechanisms for N2F8 deposited on RS-3 (h) and PVK (i), illustrating more efficient population of the SE-active state and stronger SE on RS-3, and stronger interfacial carrier loss and a weak SE pathway

on PVK. ASE, amplified spontaneous emission; SE, stimulated emission; EES, emissive excited state; GS, ground-state. ASE, gain and loss measurements were performed at room temperature under 337-nm pulsed excitation.

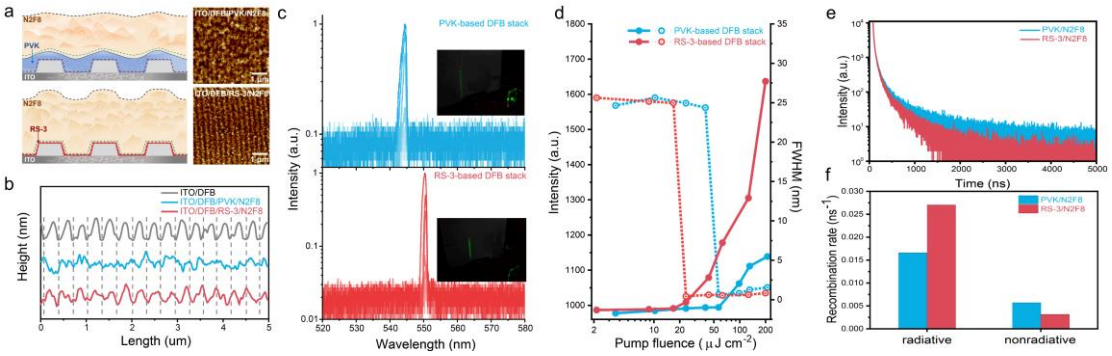


Figure 2. RS-3 preserves the DFB corrugation and reduces the optically pumped lasing threshold.

a, Schematics of N2F8 deposited on PVK- and RS-3-modified SiO_2/ITO DFB substrates (left) and corresponding AFM topographic images (right). Scale bars, 1 μm. **b,** Representative AFM height profiles of the bare ITO/DFB substrate and the ITO/DFB/PVK/N2F8 and ITO/DFB/RS-3/N2F8 stacks. **c,** Pump-fluence-dependent emission spectra of the PVK- and RS-3-based DFB stacks. The pump fluences were 3.57, 10.28, 23.67, 39.86, 56.70, 98.44, 130.68 and 210.35 μJ cm^{-2} for the PVK-based stack, and 2.15, 8.74, 16.88, 23.67, 43.54, 62.83, 126.55 and 200.05 μJ cm^{-2} for the RS-3-based stack. Insets show representative far-field emission patterns in the above-threshold regime. **d,** Peak emission intensity (filled symbols, left axis) and FWHM (open symbols, right axis) as functions of pump fluence. **e,** Time-resolved photoluminescence decay curves of PVK/N2F8 and RS-3/N2F8 films. **f,** Radiative and non-radiative recombination rates calculated from the measured PLQYs and photoluminescence lifetimes.

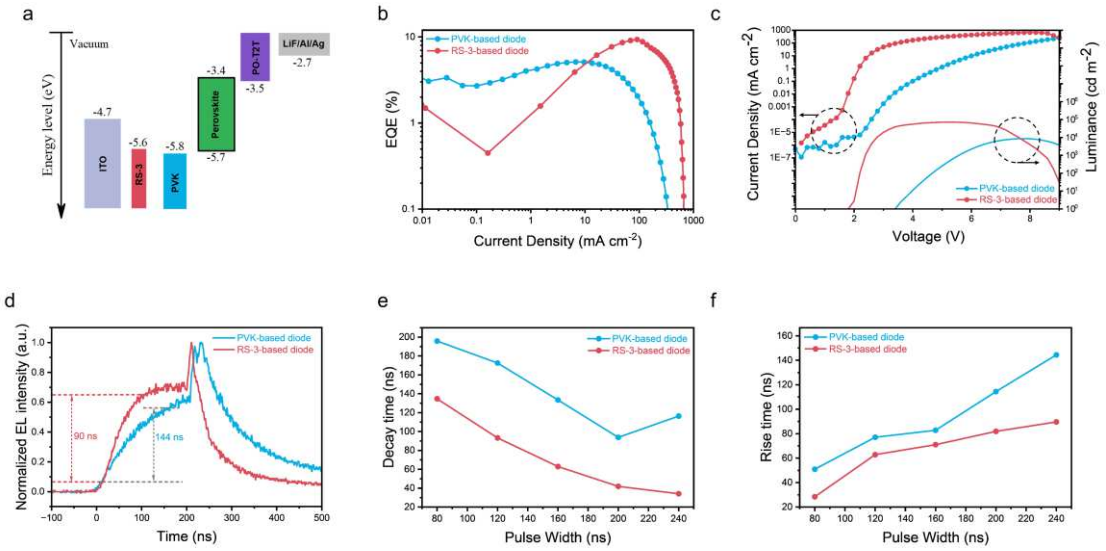


Figure 3. RS-3 promotes carrier injection and accelerates transient electroluminescence in N2F8 diodes.

a, Energy-level diagram of the ITO/HTL/N2F8/PO-T2T/LiF/Al/Ag diode, where the HTL is PVK or RS-3. **b,** External quantum efficiency (EQE) as a function of current density for PVK- and RS-3-based diodes. The maximum EQE increases from 5.1% to 9.3% after replacing PVK with RS-3. **c,** Current-density–voltage–luminance characteristics of the two devices. Symbols denote current density and solid curves denote luminance. **d,** Time-resolved electroluminescence traces under a 60-V electrical pulse with a width of 240 ns. Dashed guides indicate the extracted rise times of 144 ns for the PVK-based diode and 90 ns for the RS-3-based diode. **e,f,** Extracted electroluminescence decay times (**e**) and rise times (**f**) as functions of electrical-pulse width for PVK- and RS-3-based diodes.

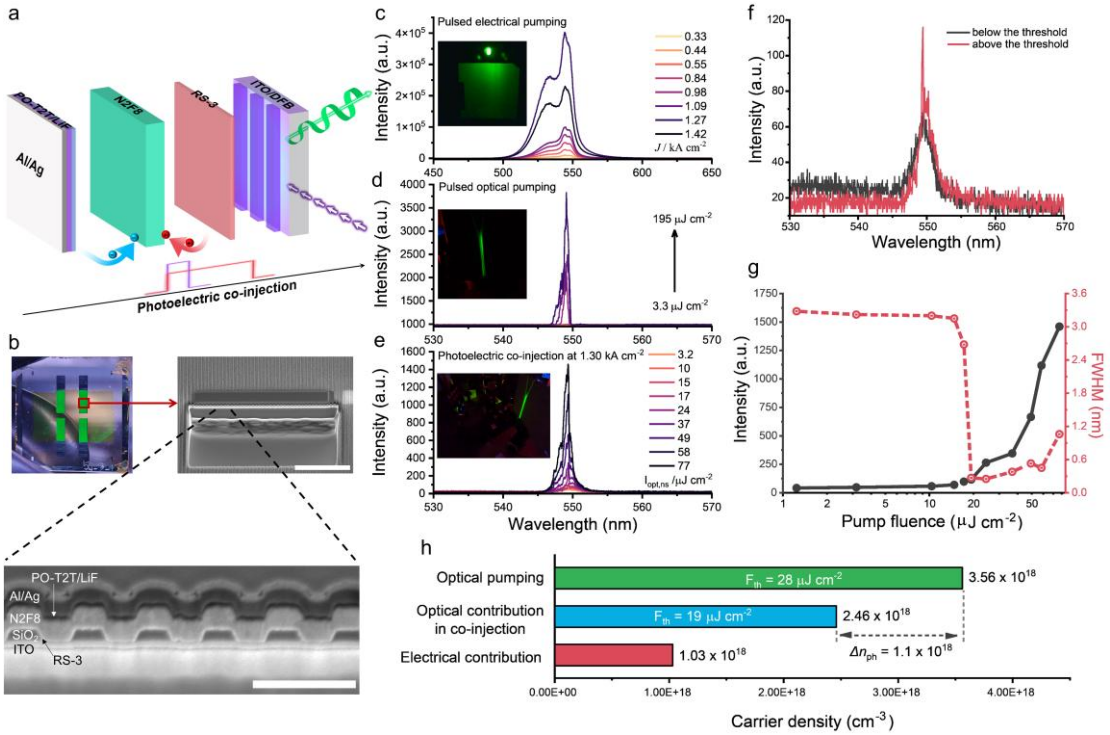


Figure 4. Room-temperature photoelectric co-injection lasing from an RS-3-based perovskite lasing diode.

a, Schematic device architecture and synchronized photoelectric co-injection configuration of the glass/ITO/SiO_2 DFB/RS-3/N2F8/PO-T2T/LiF/Al/Ag PeLD. **b,** Photograph of the fabricated device (left), tilted-view SEM image of the DFB device (top right; scale bar, 5 μm) and magnified cross-sectional SEM image showing the periodically modulated multilayer stack (bottom; scale bar, 500 nm). **c,** Electroluminescence spectra under pure pulsed electrical excitation at peak current densities from 0.33 to 1.42 kA cm^{-2}. A DFB-selected spectral feature develops near 550 nm on top of the broad electroluminescence background. No lasing threshold is assigned under electrical excitation alone. The inset shows a representative spatial emission pattern. **d,** Emission spectra of the complete PeLD under pure optical pumping at fluences from 3.3 to 195 μJ cm^{-2}. **e,** Emission spectra under synchronized photoelectric co-injection at a fixed electrical current density of 1.30 kA cm^{-2} and optical pump fluences from 3.2 to 77 μJ cm^{-2}. **f,** Representative spectra below and above the co-injection lasing threshold. **g,** Peak emission intensity (filled symbols, left axis) and FWHM (open symbols, right axis) as functions of optical pump fluence under photoelectric co-injection. The threshold decreases to 19 μJ cm^{-2} and the minimum

linewidth is 0.25 nm. **h,** Estimated carrier-density metrics at threshold. Pure optical pumping at 28 μJ cm^{-2} corresponds to a fluence-equivalent absorbed-photon density of 3.56×10^{18} cm^{-3}, whereas the optical contribution under co-injection at 19 μJ cm^{-2} corresponds to 2.46×10^{18} cm^{-3}. The reduction in the optical fluence-equivalent density is 1.10×10^{18} cm^{-3}. An effective ABC-model analysis estimates the instantaneous electrically injected carrier density immediately before the optical pulse to be 1.03×10^{18} cm^{-3}. This estimate assumes $\eta_{\mathrm{inj}} = 1$ and therefore represents an upper bound. The optical and electrical values have different temporal definitions and should not be interpreted as directly additive carrier populations.

Methods

All perovskite films and devices were fabricated in a nitrogen-filled glovebox unless otherwise specified. The molecule RS-3 and the polymer PVK were used as hole transport layers to compare their effects on optical gain, cavity morphology and electrical injection. Reference gain samples, optically pumped DFB devices, electroluminescent diodes and photoelectric co-injection laser-diode devices were fabricated using the corresponding structures described below.

Materials

Patterned SiO_2/ITO distributed-feedback (DFB) substrates, purchased from OPERA Solutions, Inc. (Fukuoka, Japan), consisted of SiO_2 gratings fabricated on ITO-coated glass and were used as received unless otherwise specified. Commercial ITO-coated glass substrates purchased from the same supplier were used for reference gain samples and electroluminescent devices.

The SAM-forming hole-transport molecule RS-3 was synthesized in-house. The detailed synthetic route, purification procedure and molecular characterization is provided in Supplementary Note 1 and Supplementary Fig. 1. For device fabrication, RS-3 was dissolved in N,N-dimethylformamide (DMF) at a concentration of 1 mg ml^{-1}. Poly(9-vinylcarbazole) (PVK) was purchased from Xi'an Polymer Light Technology Corp. (Xi'an, China) and dissolved in chlorobenzene at a concentration of 10 mg ml^{-1}.

The quasi-two-dimensional perovskite precursor solution for N2F8 was prepared by dissolving NMABr, FABr and $PbBr_2$, all purchased from Xi'an Polymer Light Technology Corp. (Xi'an, China), at a molar ratio of 2:7.5:8 in a mixed solvent of DMF and dimethyl sulfoxide (DMSO) with a volume ratio of 9:1. The total precursor concentration was 0.53 M with respect to $PbBr_2$. The solution was stirred until fully dissolved and filtered before use.

PO-T2T was purchased from Luminescence Technology Corp. (Lumtec, New Taipei City, Taiwan) and used as the electron transport material. Lithium fluoride (LiF) was

purchased from Xi'an Polymer Light Technology Corp. (Xi'an, China), whereas aluminium (Al) and silver (Ag) were purchased from Zhongnuo Advanced Material (Beijing) Technology Co., Ltd. (Beijing, China). These materials were used for thermal evaporation without further purification. Unless otherwise stated, all commercially obtained materials and solvents were used as received.

Preparation of ITO/HTL/N2F8 reference samples

ITO-coated glass substrates with an ITO thickness of 30 nm and a sheet resistance of 50-80 Ω sq^{-1} were sequentially cleaned by ultrasonication in deionized water, acetone and isopropanol for 15 min each. The cleaned substrates were dried with a nitrogen gun and treated with UV–ozone for 30 min before use. After UV–ozone treatment, the substrates were immediately transferred into a nitrogen-filled glovebox for film deposition.

PVK and RS-3 were used as HTL. For both interlayers, 100 μL of the corresponding solution was dropped onto the ITO substrate and spin-coated at 4,000 r.p.m. for 40 s, followed by thermal annealing at 120 °C for 30 min. The PVK solution was prepared in chlorobenzene at 10 mg mL^{-1}, whereas the RS-3 solution was prepared in DMF at 1 mg mL^{-1}.

The N2F8 perovskite layer was deposited on top of the HTL-coated substrates by a two-step spin-coating process. A 100 μL aliquot of the N2F8 precursor solution was dropped onto the substrate, followed by spin coating at 500 r.p.m. for 10 s and then at 7,800 r.p.m. for 50 s. During the second high-speed step, 135 μL of ethyl acetate was dropped as the antisolvent 5 s after the start of spinning. The resulting films were annealed at 80 °C for 30 min. All film-deposition and annealing steps were carried out in a nitrogen-filled glovebox.

The resulting ITO/HTL/N2F8 stacks, where HTL denotes either PVK or RS-3, were used as non-resonant reference samples for steady-state absorption, photoluminescence, PLQY, TRPL, ASE, net-gain, optical-loss and TA measurements.

Fabrication of DFB substrates and DFB devices

SiO_2/ITO DFB substrates were fabricated on ITO-coated glass. The substrates were sequentially ultrasonicated in detergent, water, acetone and isopropanol and treated with UV-ozone. A 50-nm SiO_2 layer was RF-sputtered at 100 °C under Ar (0.66 Pa, 100 W). Following HMDS treatment, an approximately 70-nm ZEP520A-7 resist was patterned by electron-beam lithography and developed in ZED-N50. The pattern was transferred into SiO_2 by CHF_3 plasma etching, followed by O_2 plasma removal of the residual resist. SiO_2 was completely removed from the grating grooves to expose the underlying ITO and maintain electrical conductivity.

The grating period was designed to be 300–310 nm according to the DFB Bragg condition:

$$m\lambda_B = 2n_{eff}\Lambda$$

where λ_B is the Bragg wavelength, n_{eff} is the effective refractive index of the guided mode, Λ is the grating period and m is the diffraction order. For the second-order DFB cavities used in this work, m = 2.

The grating period was therefore selected to match the emission wavelength of the N2F8 perovskite near the green spectral region. The DFB gratings had a duty cycle of approximately 50% and a grating depth of approximately 50 nm.

Before film deposition, the SiO_2/ITO DFB substrates were cleaned using the same procedure as the planar ITO substrates. Briefly, the substrates were sequentially ultrasonicated in deionized water, acetone and isopropanol for 15 min each, dried with a nitrogen gun and treated with UV–ozone for 30 min. The cleaned substrates were then transferred into a nitrogen-filled glovebox.

PVK, RS-3 and N2F8 films were deposited on the SiO_2/ITO DFB substrates using the same spin-coating and annealing conditions as those used for the planar ITO/HTL/N2F8 reference samples. Specifically, PVK or RS-3 was first spin-coated as the hole transport layer, followed by deposition of the N2F8 perovskite layer using the two-step spin-coating process with ethyl acetate as the antisolvent. The resulting SiO_2/ITO DFB/HTL/N2F8 structures were used for morphology characterization and

optically pumped DFB lasing measurements.

Fabrication of electroluminescent and DFB laser-diode devices

Two types of electrical devices were fabricated in this work: planar electroluminescent devices and DFB laser-diode devices. For planar electroluminescent devices, the device structure was ITO/HTL/N2F8/PO-T2T/LiF/Al/Ag, where the HTL was either PVK or RS-3. For DFB laser-diode devices, the device structure was glass/ITO/SiO_2 DFB/RS-3/N2F8/PO-T2T/LiF/Al/Ag. The active area of the planar electroluminescent devices was 0.08 cm^2. The active area of the DFB laser-diode devices was 300 μm × 100 μm, corresponding to 3.0×10^{-4} cm^2.

For both device types, the deposition of the HTL and N2F8 layers followed the same procedures described above. After deposition of the perovskite layer, the samples were transferred into a vacuum thermal evaporation system for deposition of the electron-transport layer and electrodes. Thermal evaporation was started when the chamber pressure reached approximately 1×10−5 Pa. PO-T2T and LiF were deposited at evaporation rates of 0.2 Å s^{-1} and 0.6 Å s^{-1}, respectively, with a substrate rotation speed of 15 r.p.m. Al and Ag were subsequently deposited at an evaporation rate of 2 Å s^{-1}. Overall, unless otherwise specified, the nominal layer thicknesses used, where applicable, in all perovskite-based samples and devices described above were: ITO, 30 nm; RS-3, approximately 3 nm; PVK, 25 nm; N2F8, 120 nm; PO-T2T, 20 nm; LiF, 1.2 nm; Al, 3 nm; and Ag, 100 nm. The SiO_2 DFB grating had a depth of 50 nm.

Optical and structural characterization

ASE, net modal gain, optical loss and optically pumped DFB lasing measurements were performed at room temperature using a 337-nm nitrogen laser (SRS NL100) with a pulse duration of 20 ns and a repetition rate of 1 kHz. The emission signals were collected by an optical fiber and coupled into the HORIBA iHR550 grating spectrometer, with a spectral resolution of 0.1 nm. For ASE measurements, pump-fluence-dependent emission spectra were recorded to extract the ASE threshold and

linewidth. Net modal gain and optical loss were measured using the VSL and variable-distance methods, respectively, and the detailed fitting procedures are described in Supplementary Note 2. Optically pumped lasing measurements were carried out on DFB devices under the same excitation source, and the lasing threshold was determined from the nonlinear increase in emission intensity together with linewidth narrowing.

Femtosecond transient absorption (fsTA) measurements were performed using a TA100 ultrafast transient absorption spectroscopy system (Time-Tech Spectra, China) driven by a 1 kHz Ti regenerative amplifier (Spitfire Ace-100F1HP, Spectra-Physics). Pump pulses at 337 nm were generated using an optical parametric amplifier (TOPAS Prime, Spectra-Physics), and a white-light continuum probe was produced by focusing part of the fundamental beam into a sapphire crystal. Transient spectra were recorded as differential absorbance (ΔA) as a function of pump–probe delay time. The pump power varied from 6 to 36 μW to analyze excitation-density-dependent carrier dynamics. The kinetic traces corresponding to ESA, GSB and SE were extracted from selected spectral windows and fitted as described in Supplementary Note 3.

TRPL measurements were performed under 337 nm femtosecond laser excitation using the Zolix Omni-λ300i TRPL measurement system. The PL decay curves were fitted to extract the average lifetime, and the radiative and non-radiative recombination rates were calculated from the PLQY and lifetime values. PLQY was measured under 337 nm excitation using the Hamamatsu PMA-12/C9920-02 absolute quantum yield measurement system.

X-ray diffraction patterns were collected using the X-ray diffractometer to compare the crystal structure of N2F8 films deposited on PVK and RS-3 interfaces. Spectroscopic ellipsometry was performed to obtain the wavelength-dependent refractive indices of PVK and RS-3 films.

The polarization degree was determined from polarization-resolved emission measurements by placing a linear polarizer (analyzer) in the collection path and rotating it through 360° in 15° increments. Before the angular scan, the analyzer transmission axis was aligned parallel to the DFB grating grooves and defined as 0°. An emission

spectrum was recorded at each analyzer angle. The polarization degree was calculated according to $P = (I_{\max} - I_{\min})/(I_{\max} + I_{\min})$, where $I_{\max}$ and $I_{\min}$ are the maximum and minimum emission intensities measured over the full angular range.

Electrical and photoelectric co-injection measurements

EQE and J–V–L characteristics were measured using the Hamamatsu PMA-12 measurement system. Direct-current electroluminescence measurements were controlled using the same power supply and control system as that used for the EQE measurements.

For pulsed electrical excitation, voltage pulses were supplied by the FPG 01-1NL250 pulse generator of the FID GmbH. The repetition rate was fixed at 1 kHz, the pulse width was tunable from 5 ns to 250 ns, and the pulse voltage was tunable from 10 to 100 V. The electrical signal was monitored using the KEYSIGHT DSOX3024T oscilloscope. The TREL signal was detected using a Thorlabs APD430A/M avalanche photodiode. The pure pulsed electrical measurement used the same electrical branch as shown in Supplementary Fig. 9, with the optical-pump branch blocked. The injected current was calculated from the voltage drop across a 1 Ω precision sensing resistor, and the current density was obtained by dividing the calculated current by the device active area.

For photoelectric co-injection measurements, the overall optical and electrical configuration is shown in Supplementary Fig. 9. The optical excitation was provided by the same 337 nm nitrogen laser used for the optically pumped lasing measurements, and the excitation spot area was controlled to be 3.0×10^{-4} cm². The relative delay between the electrical and optical pulses was controlled using a custom-designed synchronization setup incorporating a Zolix delay generator. During photoelectric co-injection, the device was electrically biased under pulsed operation while additional pulsed optical excitation was applied to the active region. The current-density-dependent threshold measurements were performed at J=0, 0.33, 0.68, 1.07 and 1.30 kA cm^{-2}, with the optical excitation geometry, pulse timing and threshold-extraction

procedure kept unchanged.

The electroluminescence spectra under pure electrical excitation were collected using the Zolix Omni-λ3028i-EMM grating spectrometer. The emission spectra under photoelectric co-injection were collected using the HORIBA iHR550 grating spectrometer. The linewidth and emission intensity were extracted from the measured spectra, and the co-injection lasing threshold was determined from the nonlinear increase in emission intensity together with the abrupt linewidth narrowing.

Supplementary Files

This is a list of supplementary files associated with this preprint. Click to download.

- Supportinginformation.docx